



Mining for osteogenic surface topographies: In silico design to *in vivo* osseo-integration



Frits F.B. Hulshof^{a,b}, Bernke Papenburg^c, Aliaksei Vasilevich^b, Marc Hulsmans^d, Yiping Zhao^c, Marloes Levers^c, Natalie Fekete^c, Meint de Boer^f, Huipin Yuan^g, Shantanu Singh^e, Nick Beijer^b, Mark-Anthony Bray^e, David J. Logan^e, Marcel Reinders^d, Anne E. Carpenter^e, Clemens van Blitterswijk^h, Dimitrios Stamatialis^a, Jan de Boer^{b,*}

^a MIRA Institute for Biomedical Technology and Technical Medicine, Department of Biomaterials Science and Technology, University of Twente, Enschede, The Netherlands

^b MERLN Institute for Technology-Inspired Regenerative Medicine, Department of Cell Biology -Inspired Tissue Engineering, Maastricht, The Netherlands

^c Materiomics BV, Maastricht, The Netherlands

^d Delft Bioinformatics Lab, Delft University of Technology, Delft, The Netherlands

^e Imaging Platform, Broad Institute of MIT and Harvard, Cambridge, MA, USA

^f MESA+ Institute for Nanotechnology, University of Twente, Enschede, The Netherlands

^g Xpand Biotechnology BV, Bilthoven, The Netherlands

^h MERLN Institute for Technology-Inspired Regenerative Medicine, Department of Complex Tissue Regeneration, University of Maastricht, Maastricht, The Netherlands

ARTICLE INFO

Article history:

Received 10 January 2017

Received in revised form

10 May 2017

Accepted 11 May 2017

Available online 12 May 2017

Keywords:

Surface topography

High-throughput screening

Bone implants

Differentiation

Micro-fabrication

Computational modeling

ABSTRACT

Stem cells respond to the physicochemical parameters of the substrate on which they grow. Quantitative material activity relationships – the relationships between substrate parameters and the phenotypes they induce – have so far poorly predicted the success of bioactive implant surfaces. In this report, we screened a library of randomly selected designed surface topographies for those inducing osteogenic differentiation of bone marrow-derived mesenchymal stem cells. Cell shape features, surface design parameters, and osteogenic marker expression were strongly correlated *in vitro*. Furthermore, the surfaces with the highest osteogenic potential *in vitro* also demonstrated their osteogenic effect *in vivo*: these indeed strongly enhanced bone bonding in a rabbit femur model. Our work shows that by giving stem cells specific physicochemical parameters through designed surface topographies, differentiation of these cells can be dictated.

© 2017 Elsevier Ltd. All rights reserved.

1. Introduction

Medical implants such as stents, hip implants and pacemakers have already made a tremendous impact on the quality of life of millions of patients. Further success can be expected if the response of the host tissue to the implant can be better controlled; often these devices fail to properly embed in the patient's tissue [1,2]. Biomaterial engineering offers a vast design space with properties such as stiffness [3], chemistry [4] and surface topography [5], all of which are known to influence cell behavior and tissue response [6].

A major challenge is to correlate all these material properties to the final tissue response. As a consequence, the current surge of innovations in biomaterial engineering is not yet altering clinical practice.

A parallel to this challenge of correlating design parameters to biological response is found in pharmacology, where quantitative structure activity relationship analysis (QSAR) is used as a strategy to explore chemical design space. The starting point typically is a protein with a validated role in disease pathophysiology; the goal is to alter a (small) molecule's structure to optimize its binding and thus its effects on the protein's activity. The interaction between molecule and protein can be described at the sub-molecular level and thus modeled and optimized. The final, optimized drug can be considered as a molecule-to-molecule therapeutic strategy.

* Corresponding author.

E-mail address: jan.deboer@maastrichtuniversity.nl (J. de Boer).

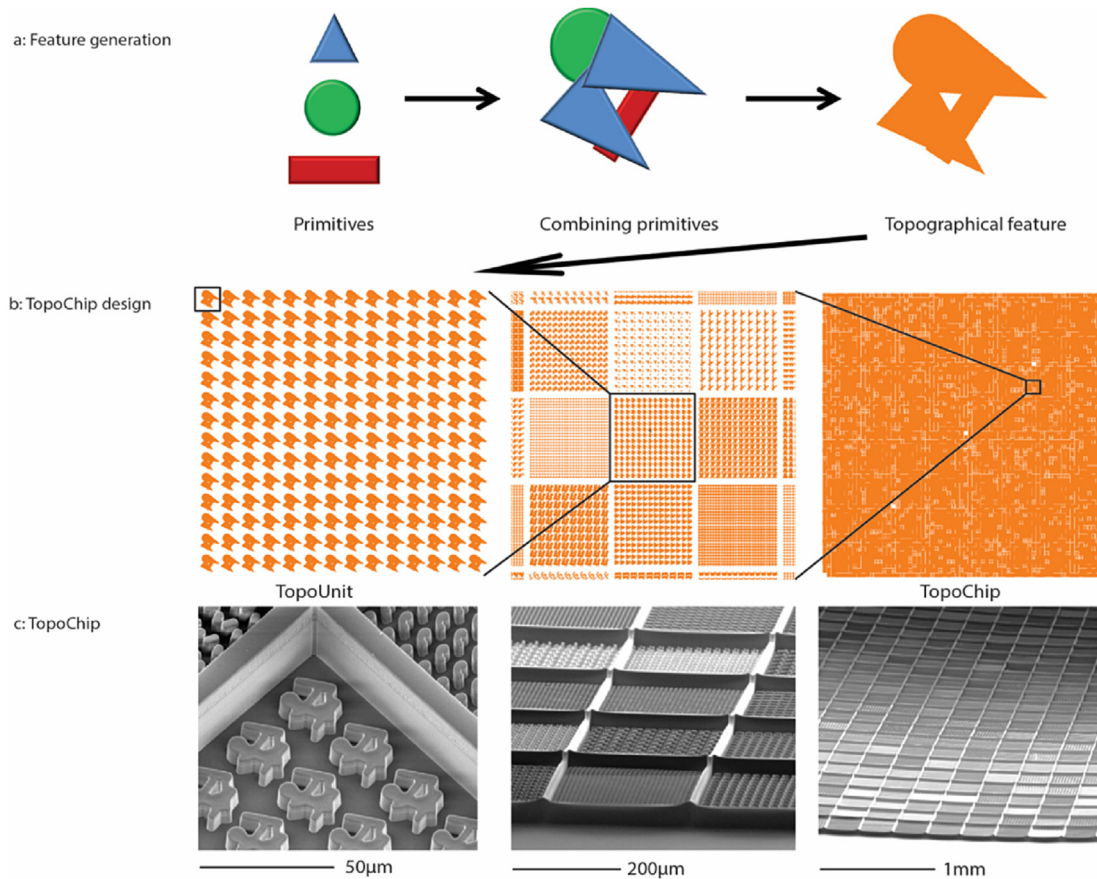


Fig. 1. TopoChip design. (a) From left to right; the 3 primitive shapes, circle, triangle and rectangle are combined in varying numbers and dimensions, to form a random shape of a topographical feature. Range of parameters within the algorithm allows a theoretical library of topographies with 150 million different possible shapes. (b) For the TopoChip design 2176 topographical features are randomly selected from the theoretical library and arrayed in $290 \times 290 \mu\text{m}^2$ TopoUnits, as well as TopoUnits without topographical features as flat reference. From left to right the illustrations zoom out from a single TopoUnit to a complete $2 \times 2 \text{ cm}^2$ TopoChip. (c) Below the illustrations are SEM images with similar scaling.

In contrast, medical implants act at the tissue level to replace damaged tissues (e.g. artificial heart valves, artificial intra-ocular lenses, or hip implants) or to control malfunctioning tissue (e.g. pacemakers, stents or abdominal wall meshes). As such, medical implant materials can be considered as a material-to-cell therapeutic strategy, in which multiple biomaterial parameters affect various aspects of cell physiology. For instance, surface topography can modulate focal adhesion formation, as well as cytoskeletal and nuclear organization [7].

Computational modeling approaches to describe quantitative material activity relationships have been used in biomaterial engineering [8–11]. For instance, partial least squares analysis of bacterial attachment to a combinatorial polymer library uncovered strong correlation between bacterial attachment and physical parameters [12]. Our prior investigations, using high-throughput screening of topographies, have shown correlations between topographical design parameters and nuclear shape features [13] and colony-forming ability of embryonic stem cells [14]. However, while strong correlations have been found *in vitro*, so far no reports demonstrate translation of these correlations, identified by high-throughput screening, to *in vivo* tissue response.

Here, we aim to demonstrate that proper selection of biomaterial surface topographies based on their parameters plus a robust *in vitro* bioassay can predict *in vivo* tissue response. We designed, produced and screened thousands of randomly selected, designed topographies on a titanium-coated TopoChip for improved osseointegration. The TopoChip platform comprises of an *in silico*

designed library of patterns with features in the range of a few to tens of microns that are reproduced into biomaterials of choice using microfabrication technologies. We applied human mesenchymal stem cells (hMSCs) as an *in vitro* cell model to identify osteogenic topographies and further tested candidates *in vivo* using a rabbit model.

This study investigates whether, similar to the pharmaceutical QSAR approach, medical implant design can be approached through computational modeling of material-cell interaction, and can be translated into an improved medical device, validated in a pre-clinical model.

2. Results

2.1. Screening identifies topographies that induce ALP expression of hMSCs

To identify topographies that improve bonding of titanium implants to bone, we produced TopoChips of poly lactic acid (PLA) films coated with a 200 nm layer of titanium (Fig. 1). Fabrication quality and reproducibility was confirmed by scanning electron microscopy (SEM, Fig. 1c).

In a pilot experiment, hMSCs with verified multi-lineage potential (Fig. S1) were seeded, grown on a TopoChip for 5 days and stained for actin and DNA. We observed a wide variety of both nuclear and actin morphologies in response to the microtopographies (Fig. 2). Within a TopoUnit (indicated by yellow box

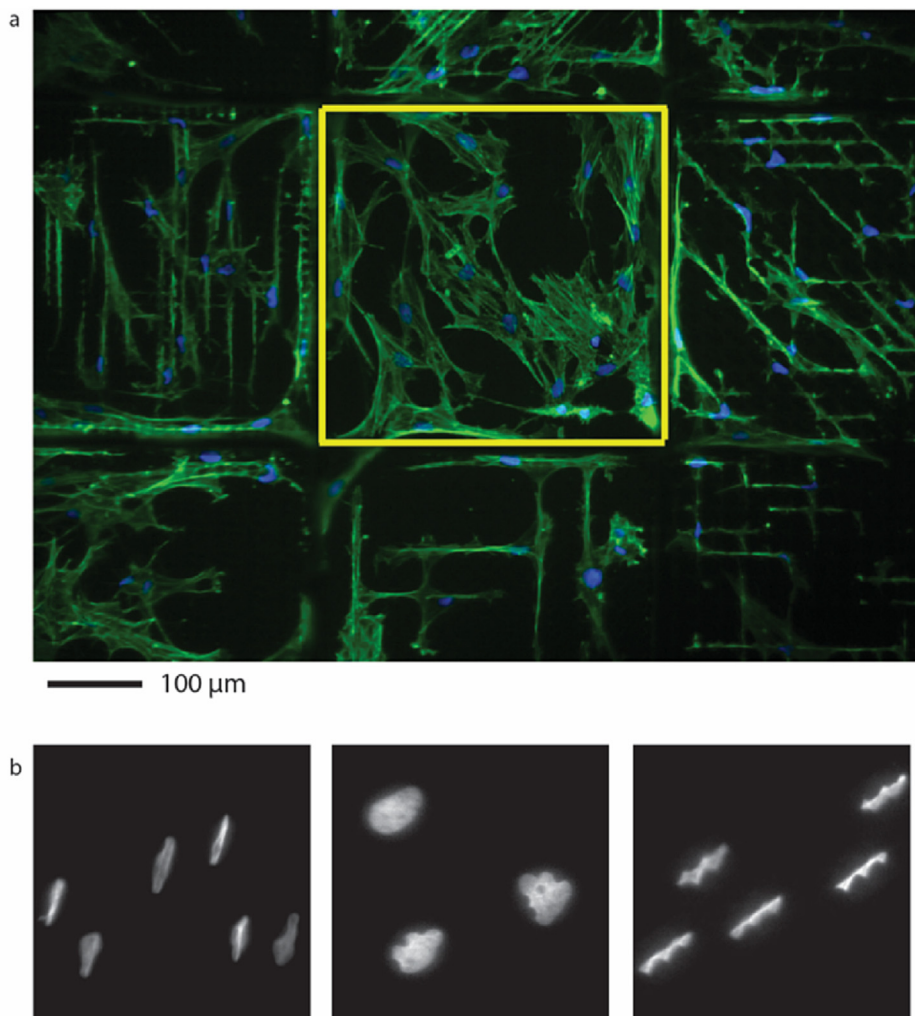


Fig. 2. Defined surface topographies included in the TopoChip cause dramatic and reproducible morphological responses in hMSCs. Morphological analysis of hMSCs cultured for 5 days on TopoChips. (a) Fluorescent micrograph of a randomly selected TopoChip region showing a variety of cellular morphologies that can be obtained by different surface topographies. Each TopoUnit (yellow square showing the outline of 1 TopoUnit) contains a unique surface topography that affects cell morphology in a robust and reproducible way. hMSCs were immunofluorescently stained for DNA (DAPI in blue) and filamentous actin (Phalloidin in green). (b) Selection of highly deformed nuclei as a reaction on surface topography. A reference image of hMSCs cultured on a non-patterned surface is shown in [Supplementary Fig. S2](#). (For interpretation of the references to colour in this figure legend, the reader is referred to the web version of this article.)

in [Fig. 2a](#)), cell morphologies typically appeared very similar.

For screening, hMSCs were seeded onto 8 titanium-coated TopoChips and cultured for 5 days after which the nuclei and filamentous actin cytoskeleton were fluorescently labeled. We also stained tissue non-specific alkaline phosphatase, because it is crucial for mineralization of bone and upregulated by many known osteogenic molecules [15].

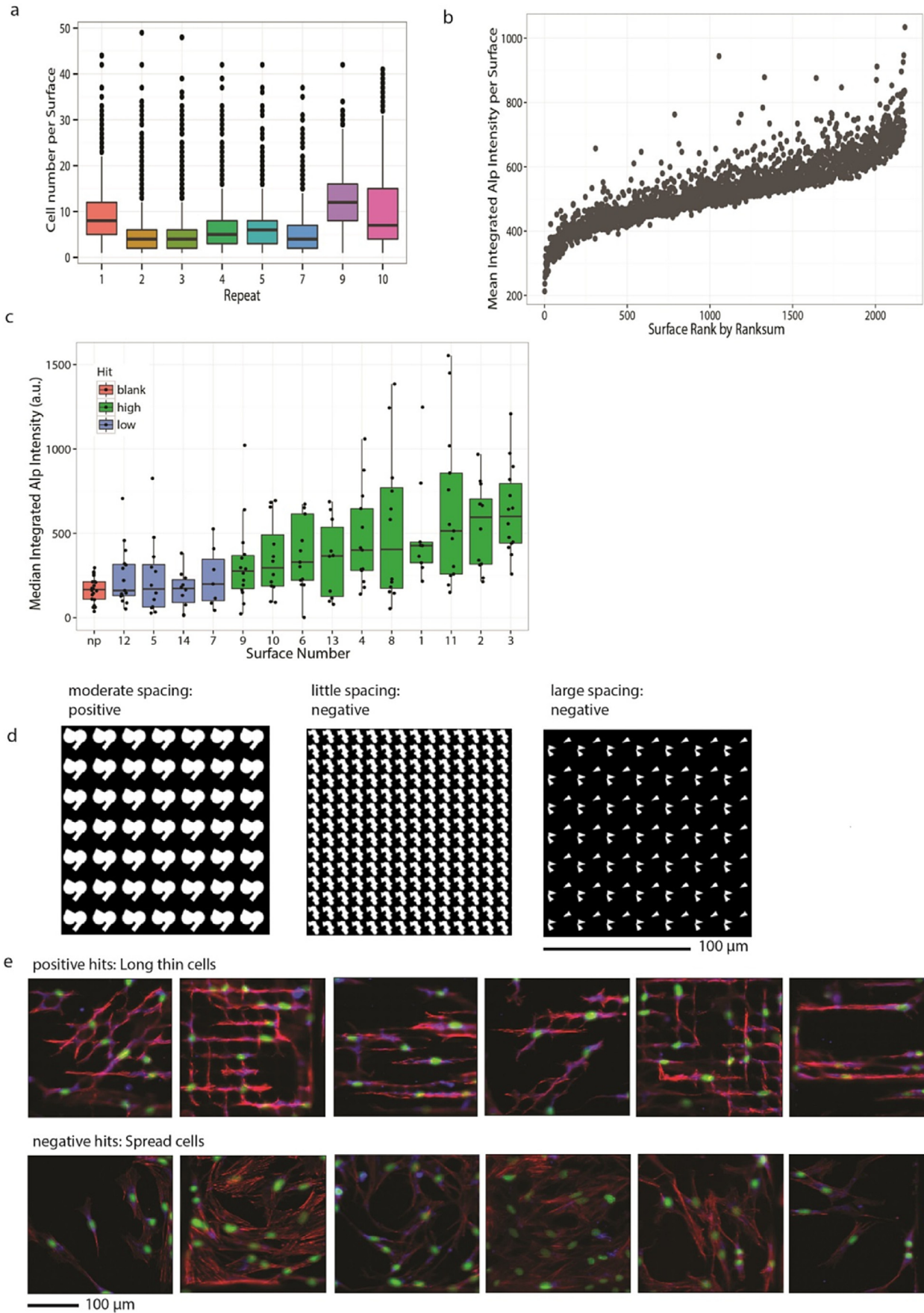
Quantitative high content image analysis demonstrates that the number of cells per unit follows a normal distribution associated with the stochastic cell seeding process ([Fig. 3a](#)) and that cell morphology is highly reproducible between replicate TopoUnits ([Supplementary Fig. S3](#)).

We identified a set of topographies that modulate ALP expression by measuring ALP intensity per cell ([Fig. 3b](#)) as compared to a non-patterned surface, which has among the lowest ALP intensity. The mean ALP expression measurements of 14 surfaces on the ends of the S curve ([Fig. 3c](#)) (9 ALP^{high}, 5 ALP^{low}) show a 2–3 fold relative difference which is very similar to the fold-induction observed when hMSCs are exposed to osteogenic molecules such as dexamethasone and BMP2.

2.2. ALP expression correlates with cell morphology and topographical shape parameters

The TopoUnits ([Supplementary Fig. S4](#)) with significantly low ALP expression, ALP^{low} units, contain either small features of several micrometers with large spacing of more than 15 μm, or large features of 10–30 μm with spacing of a few micrometers ([Fig. 3d](#)). In either case, the topographies induce flat, spread cells, similar to the non-patterned surface. In contrast, the high scoring units, ALP^{high} units, have features of 10–30 μm with a moderate spacing of 5–10 μm. The cells were confined between the structures and are relatively narrow compared to cells on flat surfaces ([Fig. 3e](#)).

To investigate the relationship between ALP level and cell shape, we used quantitative measurements of cell morphology from one hundred surfaces with the highest and lowest ALP intensity, respectively. Several cell shape parameters [16] such as cell solidity, Euler number and compactness describe the correlation between cell shape and ALP expression ([Fig. 4a](#)). A Random Forest classifier was trained with 10 fold cross validation to predict ALP expression



based on cell shapes (Fig. 4b) with an accuracy of 70%. In line with our visual observation, solidity and compactness were the most important cell shape features that were able to predict ALP expression (Fig. 4c) and could be used to separate the two surface classes (Fig. 4d).

We analyzed this morphological difference between positive and negative hits in more detail by higher-resolution confocal microscopy (Fig. 4e). In agreement with the screening experiment, the cells on the positive hit topographies are confined between the structures, leading to cells resembling a network of tubes. Cross sections of confocal image stacks (Fig. 4f) clearly show that the tube-like cells on the topographies are on average double the height (9.4 and 12 μm) of the cells on a flat surface (4.8 μm) and on the negative hit surface (6 μm).

To assess the quantitative material activity relationship between surfaces classes based on ALP expression and topographical design, we first employed a classification tree algorithm (Fig. 5a). We found that ALP^{low} or ALP^{high} surfaces clearly can be separated by pattern area, feature density and Wavenumber (WN) parameters, which relate to the spatial organization of the primitives in the feature. To further explore prediction possibility of ALP^{low} and ALP^{high} surfaces by surface design parameters we trained a model with 10-fold cross validation. We tested a variety of machine learning binary classification algorithms and found that Random Forest was the most accurate. Model performance was assessed on held-out dataset that was not used for model training. We found that ALP^{low} and ALP^{high} surfaces could be distinguished with very high accuracy (90% accuracy; area under ROC curve was 98%, Fig. 5b); a limited number of design features were needed to predict ALP expression (Fig. 5c and d). Almost all positive hits have a high pattern area (PatAr), confirming our initial visual assessment that a minimum feature size is required for the cells to be morphologically affected. In conclusion, both feature design and cell shape are highly predictive of ALP expression and machine-learning models can be trained to make these predictions.

2.3. Designed topographies instruct differentiation in hMSCs *in vitro*

To confirm that ALP^{high} units support osteogenic differentiation using more conventional molecular and cellular assays, 14 topographies were reproduced on discs with a diameter of 1.5 cm (Fig. 6a). For 7 of these (4 ALP^{high}, 3 ALP^{low}), ALP expression was verified by flow cytometry (Fig. 6b) in hMSCs after 5 days in medium without osteogenic supplements. As expected, dexamethasone induces the percentage of ALP positive hMSCs from 13 to 25%. All 4 ALP^{high} topographies have a statistically higher percentage of ALP positive cells (24–28%) compared to both the tissue culture polystyrene non-patterned control (13%) and the titanium non-patterned control (np, 18%). Further, 3 out of 4 ALP-positive surfaces display a similar or higher percentage of ALP positive cells (26–28%) than the dexamethasone supplemented positive TCPS control (25%). On the other hand, the ALP^{low} topographies have similar or lower percentage of ALP positive cells (13–22%) than the titanium non-patterned control (np, 18%).

To investigate the long-term effects of topography on osteogenesis, *in-vitro* mineralization of hMSCs was studied on ALP^{low} non-patterned control surfaces, and on ALP^{low} #7, ALP^{high} #4 and #8 (Supplementary Fig. S5). Because orthopedic implant surfaces are exposed to an osteogenic environment when implanted *in vivo*, this mineralization experiment was performed in osteogenic medium. The two ALP^{high} topographies #4 and #8 show a 2- to 3-fold increase in mineralized matrix, compared to the non-patterned (np) titanium (Fig. 6c). To test whether the enhanced mineralization corresponded to osteogenic differentiation, gene expression of the osteogenic markers osteocalcin (Ocn), osteopontin (Opn) and bone sialoprotein (Bsp) was measured after 5 weeks. Both ALP^{high} surfaces #4 and #8 showed large upregulation of gene expression (13- and 8-fold relative to the non-patterned control, Fig. 6d). Surface #7 showed intermediate values, consistent with the mineralization results. In conclusion, topography-induced ALP expression levels correlate to osteogenic differentiation and mineralization of hMSCs.

2.4. Designed topographies improve osseo-integration *in vivo*

To confirm that the topographies inducing osteogenesis of hMSCs *in vitro* also enhance osseo-integration *in vivo*, we used an orthotopic rabbit model [17,18], in which experimental implants are fixed into the proximal part of the femur. ALP^{high} topographies #1, #4 and #8, and ALP^{low} topography #14 were fabricated into solid titanium implants using micromachining technologies (Fig. 7a). As a positive control and clinical benchmark we included one of the best-documented surfaces in dental implantology, a sand-blasted and acid-etched (SLA) surface [19,20]. We included non-patterned titanium as a negative control. The resulting topographies had high resolution and reproducibility, comparable to the Ti-coated PLA topographies (Fig. 7b).

Four and eight weeks after implantation, the rabbits were sacrificed and the femurs were fixated for pull-out testing which measures the force required for detachment of the implant (Fig. 7c). The non-patterned implants (negative control) have at both 4 and 8 weeks the lowest pull-out force. At 4 weeks, all topography-featuring implants including the commercial benchmark, require between 2 and 4 times the forces required for the non-patterned implant, with ALP^{high} #1 standing out requiring over 5 times the force of the non-patterned implant. At 8 weeks, the non-patterned implant now still requires less force to be detached compared to the best scoring topography at 4 weeks. The other topography-featuring implants, including the commercial benchmark, require about 2 times the force of the non-patterned implant (all week 8). One topography statistically (ANOVA $p < 0.05$) outperforms the non-patterned control at 8 weeks, ALP^{high} #8, requiring over 3 times the force of the non-patterned implant.

As a secondary method to assess *in vivo* response to the topographical implants, the bone-implant contact percentage (%BIC) was quantified (Fig. 7d). Non-patterned implants had a low mean BIC of around 10% at both four and eight weeks. Most non-

Fig. 3. TopoChip screen for increased ALP expression led to identification of osteogenic surface topographies. hMSCs cultured on titanium coated TopoChips in basic medium for 5 days before fixation and staining for DNA, filamentous actin and Alkaline Phosphatase. (a) Distributions of cell number per TopoUnit, for each TopoChip in the screening experiment. (b) Average ALP expression per cell for each TopoUnit, ranked by Ranksum criteria. (c) Boxplot including raw data point of the median integrated ALP signal intensity from TopoUnit replicates containing surface topographies identified in the screen as high or low scoring. (d) Correlation between topographical feature spacing and ALP expression. TopoUnits with no effect on ALP expression contain topographies with either little or large spacing between the topographical features, while the highest upregulation of ALP expression was observed in TopoUnits with a moderate spacing. Images represent the 3 groups of typical topographical shapes identified as a hit (low and high ALP expression). (e) Immunofluorescent images of a single TopoUnit area containing hMSCs (filamentous actin in red, DNA in green and ALP in blue), showing the correlation between cell spreading and ALP expression. TopoUnits with the highest upregulation of ALP expression typically contain elongated and thin cells, while a more spread cell morphology was found in TopoUnits with low ALP expression. (For interpretation of the references to colour in this figure legend, the reader is referred to the web version of this article.)

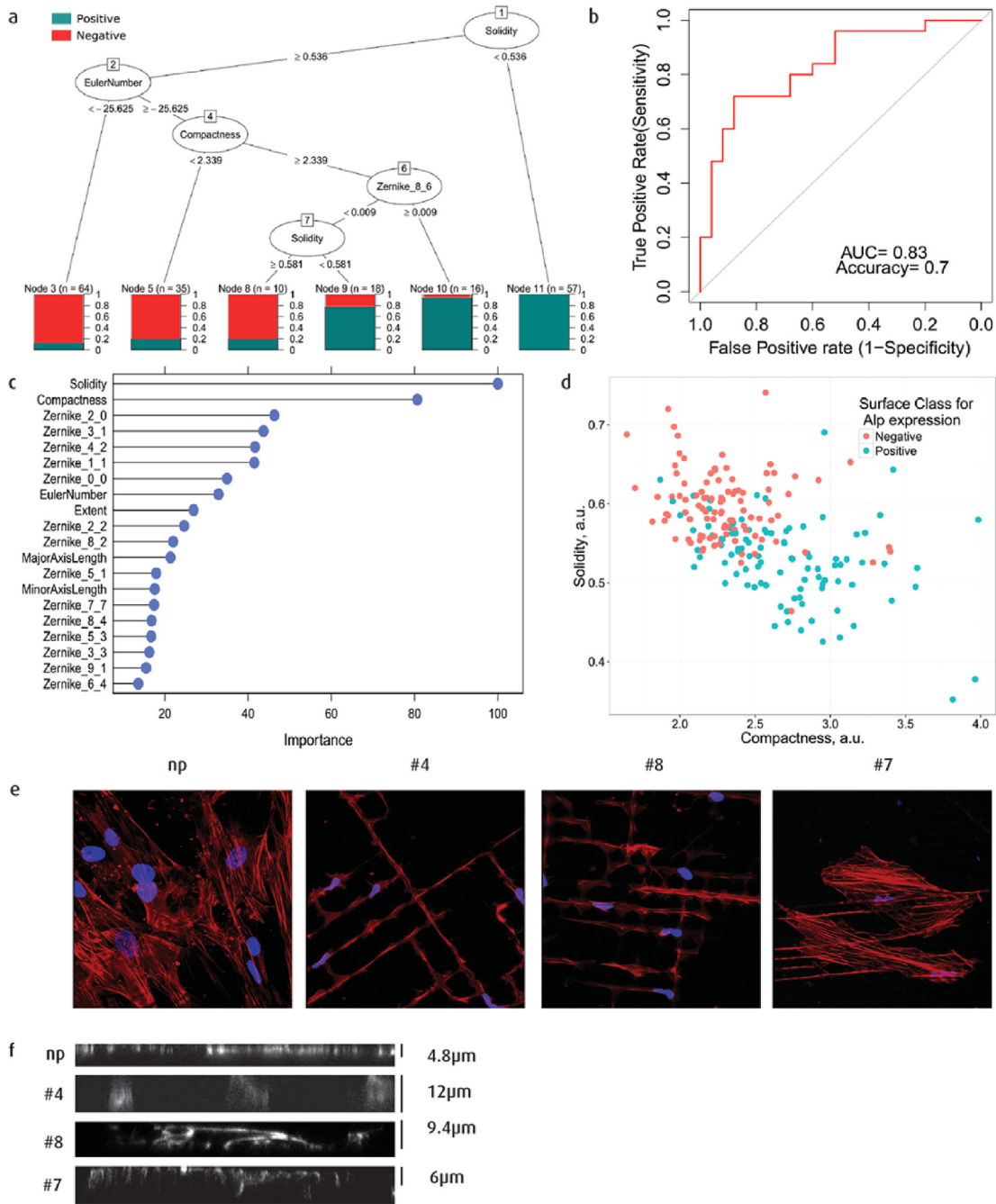


Fig. 4. Identification of cell morphological parameters that increase ALP expression. (a) Regression tree distinguishing negative and positive surfaces by cell shape parameters. Each branch of the tree diagram introduces a new morphological feature to divide the remaining cell morphologies as high or low scoring unit. After each node, the fraction of positive (high ALP) versus negative (low ALP) cell morphologies are shown. (b) ROC curve showing the prediction performance of the random forest classification algorithm. (c) Bar diagram showing the importance of cell morphology parameters as predicting factors for ALP expression. (d) Scatter plot showing the distribution of solidity and compactness parameters for topographies with the highest (blue; top hits) and lowest (red; bottom hits) expression of ALP. (e) Confocal images of hMSCs cultured on high ALP hit topographies #4, #8 and the low ALP hit topography #7. Filamentous actin in red, DNA in blue. (f) Height of cells cultured on the hit topographies measured using confocal z-stack cross sections. The definitions of the Cell profiler features (Zernike, EulerNumber, etc.) are presented in [Supplementary Table 1](#). (For interpretation of the references to colour in this figure legend, the reader is referred to the web version of this article.)

patterned samples had large areas of fibrous tissue (Fig. 7e). SLA implants and the ALP^{high} topographies, #1, #4, #8, all have a higher BIC at four weeks and a statistically significantly (ANOVA $p < 0.05$) higher BIC than the non-patterned implant at eight weeks (Fig. 7f). The ALP^{low} #14 had a very poor %BIC. Upon closer inspection of the histological samples, small pieces of titanium are visible in the fibrous tissue (Fig. 7g). It appears that the pieces of titanium have

broken off due to the high aspect ratio of this particular topography which could explain the poor %BIC. Overall, the data does not show a strong relation between the pull out force and the BIC which is probably caused by biological variability.

Taken together, *in silico* designed topographic surfaces that induce osteogenic differentiation *in vitro*, improve at similar levels bone bonding of titanium surfaces *in vivo*.

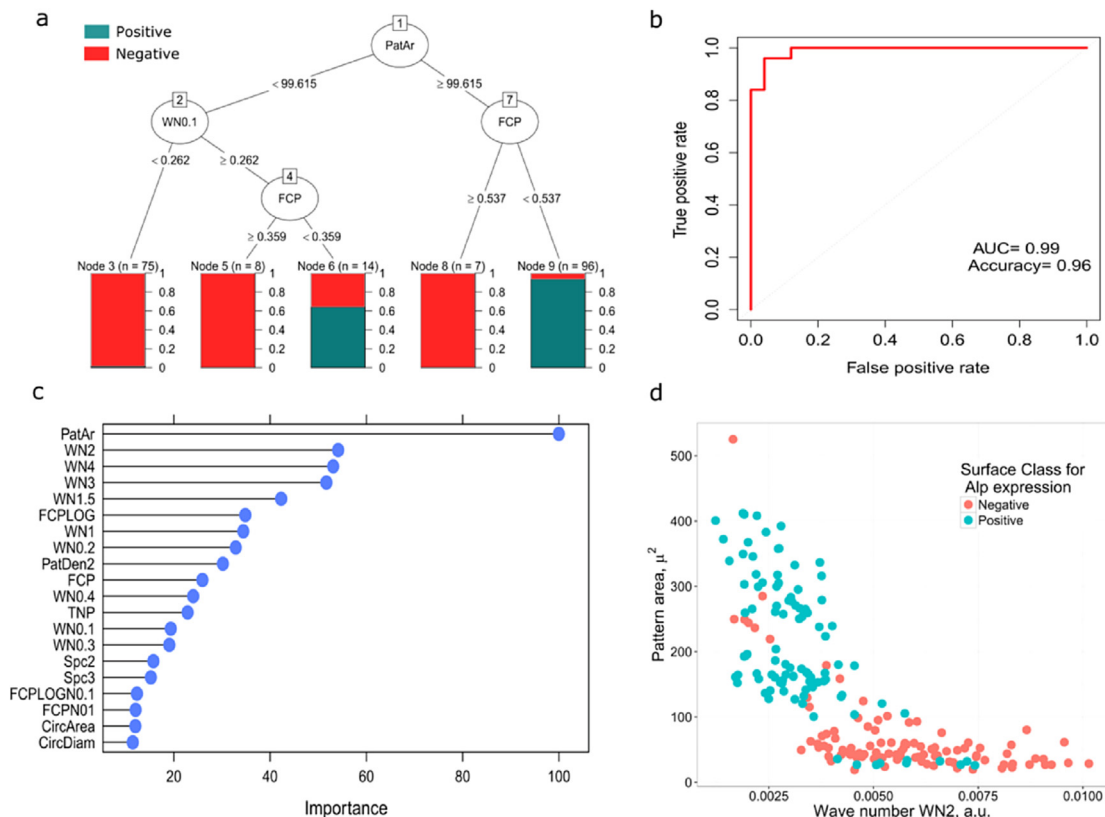


Fig. 5. Identification of topographical feature design parameters that increase ALP expression. (a) Regression tree distinguishing high and low ALP surfaces by topographical feature design parameters. Each branch of the tree diagram introduces a new morphological feature to divide the remaining design parameters as high or low scoring unit. After each node, the fraction of positive (high ALP) versus negative (low ALP) design parameters are shown. (b) ROC curve showing the prediction performance of the random forest classification algorithm. AUC is the area under the curve which indicated the predictive power of the model (c) Bar diagram showing the importance of topographical feature design parameters as predicting factors for ALP expression. (d) Scatter plot showing the distribution of Pattern area and wavenumber2 parameters for topographies with the highest (blue; top hits) and lowest (red; bottom hits) expression of ALP. The definitions of the shape features of the topographies (ParAR, WN2, etc.) are presented in [Supplementary Table 2](#). (For interpretation of the references to colour in this figure legend, the reader is referred to the web version of this article.)

3. Discussion

The study of cell-material interactions faces a world of almost limitless design parameters, thanks to rapidly evolving engineering possibilities. High-throughput screening tools have been developed for multiple material properties such as bulk chemistry [21], surface chemistry [12,22], 3D architecture [23], adhesion molecule composition [24] and surface topography [25]. Implementation of these newly developed screening platforms in combination with computational analysis could facilitate translation of *in vitro* screening to improved performance of biomaterials *in vivo*. This report shows a complete route spanning from *in silico* biomaterial design, through *in vitro* high-throughput screening, to *in vivo* functionality.

In our work, we used ALP expression in human mesenchymal stem cells as an *in vitro* bio-assay, because in earlier work it has been shown to correlate to *in vivo* bone formation [26]. In the literature, there are important attempts for applying of *in vitro* assays to predict *in vivo* response and/or performance [27]. In fact, several *in vitro* studies used ALP as a marker for the osteogenic process, and very successfully, in many cases. Our work shows that ALP expression correlates **one on one** with *in vitro* mineralization and osteogenic marker gene expression. Moreover, we found that surfaces with low ALP expression have low bone contact and surfaces with high ALP expression have high bone contact. These first results cannot fully prove causality between improved osteogenic differentiation of human MSCs

in vitro and improved bone bonding in the rabbit femur, however, they still indicate that our *in silico* surface topography design combined with a high-throughput readout can contribute to making predictions that translated from bio-assay to *in vivo* bone bonding.

Our finding that surface topography induces ALP expression in MSCs and induces *in vivo* bone bonding is in line with previously reported data. For instance, the relevance of micro-roughness on bone bonding has been advocated by Davies [28]. Dalby et al. [5] have reported that nano-sized pits induce osteogenic differentiation. Silverwood and co-workers [29] further describe effects of nanotopography on osteoclastogenesis. Similarly, we and others have previously reported on the correlation between micro-roughness of porous calcium phosphate implants and osteo-induction. In a study that we recently published, genes which were found to be correlated to bone formation *in vivo*, could be induced *in vitro* by micro-roughness [30].

In this work we did not investigate the underlying mechanisms of topography induced osteogenesis. The literature has proposed many (interconnected) molecular mechanisms such as PKA signaling [32], integrin signaling [31], and the YAP/TAZ pathway activation [33]. Furthermore, alignment and elongation of hMSCs by micro-grooves increases histone acetylation [34], which might result in osteogenic differentiation because the inhibition of histone deacetylases (HDACS) activity was previously described to increase ALP expression and mineralization of hMSCs [35].

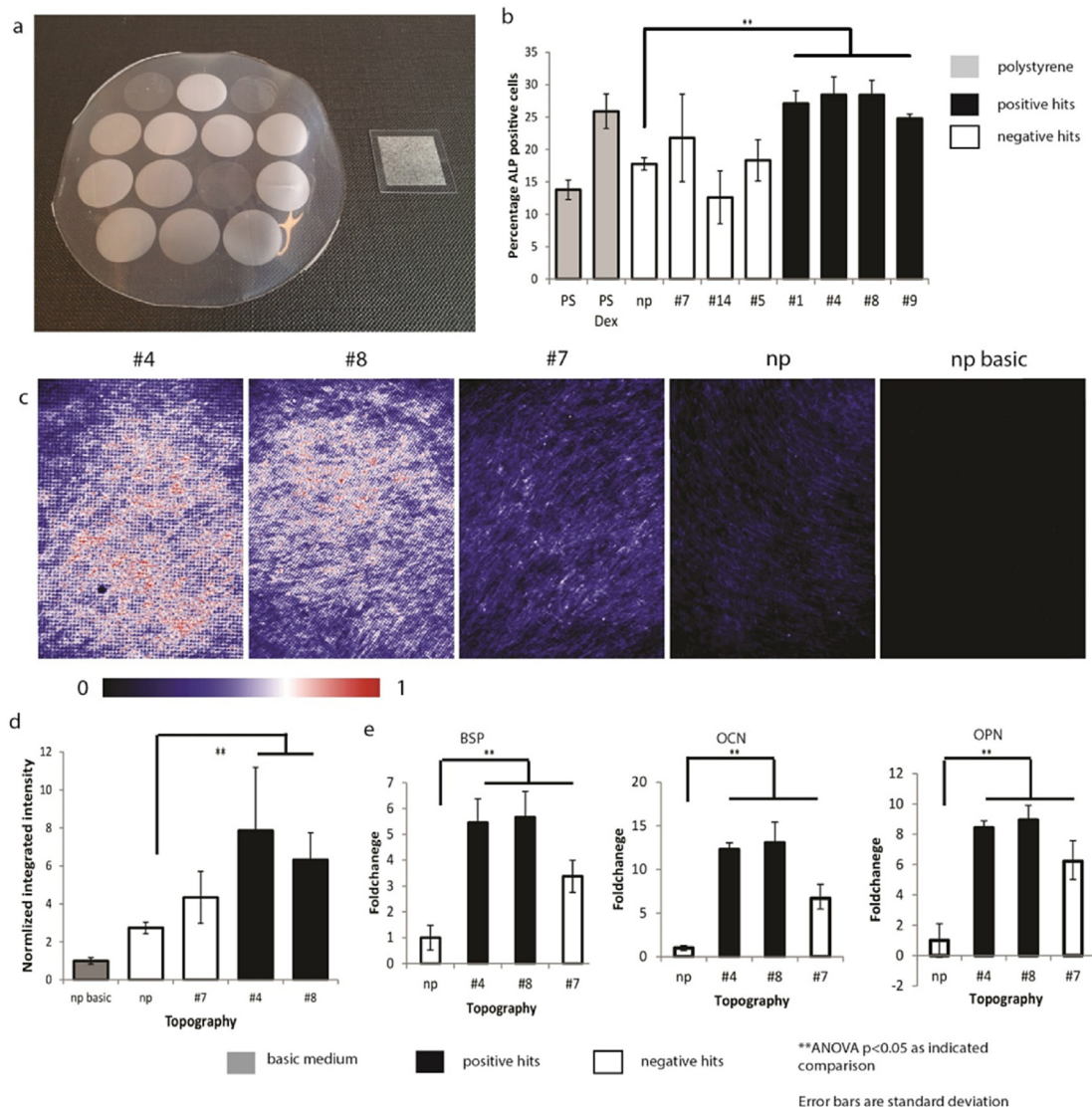


Fig. 6. In vitro characterization of the osteogenic potential of ALP screen hit topographies. (a) Topography enhanced surface areas of 7 selected hit TopoUnits were enlarged from $290 \times 290 \mu\text{m}$ (right) to circles of 1.5 cm diameter (left) to allow 12-well-plate based cell culture for further *in vitro* characterization. (b) Flow cytometry of hMSCs cultured on hit topographies for 5 days in basic medium. Bars show the mean percentage of ALP-positive cells. ALP-positive cells are defined as those cells expressing surface ALP at a higher median fluorescence intensity relative to the specific isotype control. Means are based on three measurements, error bars show standard deviation. (c) Signal intensity representation of fluorescent micrographs of hMSC mineralization visualized by tetracyclin after 5 weeks of culture under osteogenic conditions. Red and white represent high tetracyclin intensities as measured on hit topographies #4 and #8. Blue and black represent little or no signal as measured on #7 and non-patterned. (d) Mineralization was quantified using the integrated intensities of the tetracyclin signal of 15 images from 3 samples for each topography. Bars show mean integrated intensities, error bars show standard deviation. (e) Qpcr comparison for osteopontin (OPN), osteocalcin (OCN) and bone sialoprotein (BSP) transcripts from hMSCs cultured for 5 weeks on hit topographies after 5 weeks under osteogenic conditions. (For interpretation of the references to colour in this figure legend, the reader is referred to the web version of this article.)

4. Conclusions and outlook

In this work, we demonstrated clear correlations between topographical feature design vs. ALP expression, ALP expression vs. hMSC mineralization, and mineralization vs. *in vivo* bone bonding. We also have established a database of well described correlations between surface topography and hMSC differentiation, we can further explore the areas of design space not yet covered in this screen. Using permutations based on the successful designs, we can take an evolutionary approach to material engineering, using genetic and evolutionary algorithms combined with iterations of TopoChips production and screening.

While a screening approach – such as that used in this paper – is useful for finding optimized responses of cells to biomaterials, we also need to understand the molecular mechanisms involved to fully empower the field of bioactive materials. To this end, clinically

relevant phenomena such as osteo-induction of calcium phosphate ceramics, anti-fouling of polymers and pseudo-tumor formation in metal hip implants may be instructive in understanding the molecular and biological mechanisms because their resulting pathology can teach us lessons normal biology cannot. This approach of combining of knowledge of life at the biomaterial interface and computational design of biomaterial parameters could facilitate the introduction of bio-active surfaces to the clinic.

5. Materials and methods

5.1. Fabrication

5.1.1. TopoChip design and fabrication

The complete design and fabrication of the TopoChip is described in detail elsewhere [25]. In summary: The *in silico* design

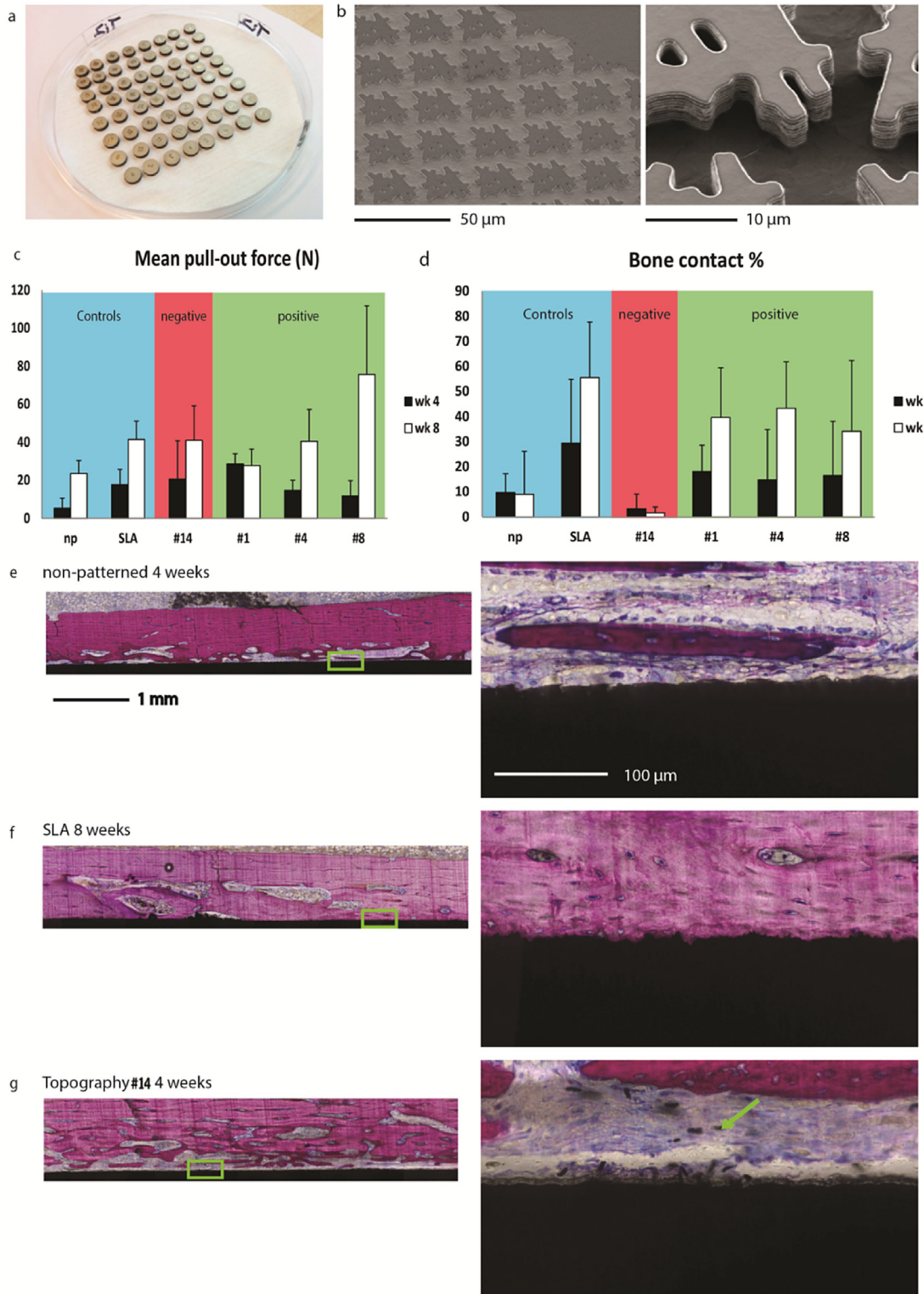


Fig. 7. In vitro characterized osteogenic surface topography shows increased bone bonding *in vivo*. (a) Solid titanium discs were enhanced with the hit topography surface structures for *in vivo* implantation. (b) SEM images of a hit topography micro-machined in a solid titanium disc. Two magnifications show the reproducibility of the topographical features as well as the topographical feature shape quality. (c,d) Mean pull-out force and bone contact percentage of the topography enhanced titanium discs from rabbit femurs 4 (black bars) and 8 weeks (white bars) after implantation. The blue shaded region of the graphs include the non-patterned reference and the clinical sand blasted, acid etched benchmark, red the topography identified as non-osteogenic, and green the topographies identified as osteogenic. Error bars represent the standard deviation. Typical histology images of a bone slice with (e) a non-patterned substrate after 4 weeks of implantation, (f) a SLA substrate after 8 weeks of implantation and (g) a low ALP hit topography #14 substrate after 4 weeks of implantation. Note: yellow arrow indicates titanium particles in the tissue. (left) An overview of entire width of the implant. (right) A magnified area from the implant, indicated with a white box in the left image. Methylene blue and basic fuchsin staining to visualize the cells and expression of an osteogenic marker and in black the titanium substrates. Representative images of bone slices from the other topographies (#1, #4 and #8) are shown in [Supplementary Fig. S6](#)).

of the TopoChip is generated using an algorithm that combines the primitive shapes: triangle, circle and rectangle to generate complex shapes. The primitive shapes “triangle, circle, rectangle” were chosen because the stochastic combination of these shapes in varying orientation, numbers and sizes results in the generation of nearly any possible shape. The *in silico* design was used to create a chromium mask for photolithography. The micro patterns were etched from the silicon wafer, by directional reactive ion etching (DRIE), generating a silicon master mould for hot embossing. To facilitate demoulding, the master was coated with a ‘non-sticky’ layer of perfluorodecyltrichlorosilane (FDTS) (ABCR, AB111155). The master was subsequently used for hot embossing of PLA films (250 μm thick) (Folienwerk Wolfen GmbH) using an Obducat nanoimprint device. Imprinting was carried out at 120 °C with 30 bars of pressure for 10 min. Demoulding took place after cooling down to 80 °C. The PLA TopoChips and up-scaled surfaces were coated with 200 nm Titanium by sputter coating at a sputtering rate of 6 nm/min.

5.1.2. Titanium implant fabrication

The Ti implants were fabricated using micromachining technologies. An outline of the fabrication scheme is illustrated in the [Supplementary Fig. S7a](#). Annealed Ti plates of 99.6% purity of 150 mm \times 150 mm and thickness of 2 mm were bought from Goodfellow, UK. (A) Ti plates were first cut by laser into 100 mm diameter substrates. After a pre-polish step using polishing paste, the Ti substrates were final polished to achieve a roughness of about 10 nm by chemical mechanical polishing (CMP Mecapol E460, Cabot SemiSpurse 25 slurry; $\text{H}_2\text{O} = 1:2$) for about 60 min. (B) After ultrasonic cleaning in demi (DI) water for 60 min, in acetone for 30 min and in isopropanol (IPA) for 30 min, 780 nm SiO_x was deposited by plasma enhanced chemical vapor deposition (PECVD, Oxford Plasmalab system 80). (C) The lithography step was performed by using positive photoresist OIR 908-12 (Arch Chemical, Inc). After exposure (EVG 620) and development (OPD 4262, Arch Chemical, Inc), the Ti substrates were hard baked on a hot plate at 120 °C for 30 min. (D) The SiO_x layer was etched by directional reactive ion etching (DRIE, Adixen AMS 100 DE). After stripping the photoresist in Oxygen (O_2) plasma (Tepla 300E), (F) the Ti substrates were etched using an alternation of an etching step of the etchant combination of $\text{Cl}_2/\text{BCl}_3/\text{Ar}$ plasma and an oxidation step by O_2 plasma (Oxford Plasmalab system 100) to receive a structure depth of about 10 μm . (G) The SiO_x masking layer was removed in 2 min using the same method as in step (D).

Individual Ti samples were cut out by electric discharge machining (EDM, Charmilles, Switzerland). The fabricated Ti substrates were coated beforehand with AZ 9260 resist for surface protection. Polytetrafluoroethylene (PTFE) caps were designed and fabricated CNC machining to avoid interlocking from lateral bone attachment as well as for the easiness of fixture attachment for tensile testing. The illustrations of a Ti implant with its PTFE cover are shown in the [Supplementary Fig. S2b](#). To obtain a tight fit of the PTFE cover to the Ti implant, the PTFE cover has an outer diameter of 7.05 mm, wall thickness of 0.4 mm and inner height of 1.90 mm. A through hole of 4 mm diameter was made for fixture fixation during tensile test. Finally, the implants were ultrasonic cleaned in acetone for 1 h and followed by Isopropanol for 1 h.

5.2. In vitro experiments

5.2.1. Cell culture

HMSCs (donor 8F3543, Lonza) were cultured in basic medium consisting of α MEM (Gibco) supplemented with 10% fetal bovine serum (Lonza), 2 mM L-glutamine (Gibco), 0.2 mM ascorbic acid (Sigma Aldrich) and 100 U ml^{-1} penicillin +100 g ml^{-1}

streptomycin (Gibco). Osteogenic medium contains basic medium with 10^{-8} M dexamethasone (Sigma Aldrich) and 0.01 M β -glycerol phosphate (Sigma Aldrich). Adipogenic consisted of DMEM (Gibco) supplemented with 100 U/ml penicillin +100 $\mu\text{g}/\text{ml}$ streptomycin (Gibco), 10% foetal bovine serum (Lonza), 0.2 mM Indomethacin (Sigma Aldrich), 0.5 mM IBMX (Sigma Aldrich) 10^{-6} M dexamethasone (Sigma Aldrich) and 10 $\mu\text{g}/\text{ml}$ Insulin (human, Sigma Aldrich). In all experiments, medium was refreshed every two days.

5.2.2. TopoChip staining and imaging

Prior to seeding, titanium-coated TopoChips are wetted for a minimum of 2 days in basic medium at 37 °C and at in a 5% CO_2 atmosphere; wetting is prolonged due to hydrophobic properties of patterned surfaces. For the screening experiment eight TopoChips were and seeded with passage 4 hMSCs (Lonza) at a density of 3000 cells/ cm^2 . The conditions of the screening experiment were carefully chosen to have the cells in a sub confluent state to allow segmentation of the cells after imaging. After 5 days of culture in basic medium, the cells were washed in phosphate buffered saline (PBS, Sigma Aldrich) and fixated in 70% ethanol and stained for ALP, cell nuclei and cytoskeleton. After fixation the cells were incubated with blocking buffer, consisting of 2% bovine serum albumin (BSA, Sigma Aldrich) in PBS for 30 min followed by primary antibody incubation of 2 h with 1:50 anti-ALP(sc137213, Santa Cruz Biotech) in blocking buffer. After washing with PBS 4 times, the cells were incubated with 1:100 Goat-anti-mouse-Alexa594 (Life Technologies) in blocking buffer for 1h, followed by 4 further PBS washings and incubation of 1:100 Phalloidin-Alexa488 (Life Technologies) in blocking buffer. Next, after washing with PBS 4 times nuclear staining with 1:10,000 4',6-Diamidino-2-phenylindole (Dapi, Life technologies) was done. Finally the TopoChips were mounted on coverslips with Mowiol 4-88 (Sigma Aldrich) after 2 PBS washes.

After sample drying, the chips were imaged using a BD Pathway 435 automated fluorescence microscope. A total of 4356 images (one for each TopoUnit) were acquired for each chip and fluorescence channel. All images were combined into a large montage of 62,964 by 62,964 pixels (3964 megapixels).

5.2.2.1. Image analysis. Image analysis is described in detail elsewhere [13]. In summary, custom matlab scripts were used for flat-field correction, image normalization and background subtraction. Quality control features were calculated and used to detect outliers. From the large montage each original image was cropped into separate images of 800 \times 800 pixels. For each of the TopoUnit images, CellProfiler [16] was used to obtain the cell morphology measurements. Among these morphological measurements made in CellProfiler are the Zernike features and Euler numbers which are abstract measurements of shape ([Supplementary Table 2](#)). To prevent influence of the walls on the cell morphology measurements, cell touching the walls were filtered out of the dataset. The DAPI channel was used to recognize nuclei, using the Otsu Adaptive thresholding method. Subsequently, each of these nuclei was used to initiate the search for a corresponding cell, by making use of the phalloidin-Alexa488 staining by Otsu adaptive thresholding and the provided propagation algorithm. Measurements were performed on the resulting shapes. Within the defined individual cell areas, ALP intensities were determined by measuring the maximum ALP intensity, the integrated ALP intensity and the integrated ALP intensity corrected for actin intensity. Hit rankings were made by using the Mann-Whitney *U* test.

5.2.3. Statistical analysis

To identify the surface design parameters that can influence ALP expression, the 100 surfaces with the highest ALP expression and the 100 surfaces with the lowest ALP expression were selected. To

classify the topographies that had a positive or negative effect on the Integrated Intensity of the ALP signal, a classification trees algorithms from “rpart” package ver. 4.1 [36] that was run in R ver. 3.1.2 [37] was used. The classification tree was visualized by this “partykit” package ver. 1.0 [38]. The Random Forest algorithm [39] was used to create the predictive model. The accuracy was depicted by the receiver operating curve (ROC), which illustrates the performance if a binary classifier by plotting the true positive rate, against the false positive rate, at various threshold settings. In order to have a training set for testing accuracy of the model, the data set was split in to 2 parts. The first part contained 75% of the data and was used for model training and the remaining 25% was used for model testing. The models were trained with 10 fold cross validation in “caret” package version 6 [40].

5.2.4. Flow cytometry

hMSCs were seeded at a density of 3500 cells/cm² on enlarged surfaces of the selected patterns and cultured for 5 days in basic hMSC medium without osteogenesis-stimulating compounds. As a control to the patterned surfaces, cells were also cultivated on non-patterned (flat) surfaces in basic hMSC medium with or without dexamethasone. The medium was refreshed every 2 days. Following the cell culture period, the cells were harvested and stained with an anti-human ALP antibody that was then labeled with a Phycoerythrin (PE)-labeled specific secondary antibody. Flow cytometry was performed immediately after staining using a FACSCalibur (BD Biosciences) and its CellQuest software (BD Biosciences). Every experimental condition was performed in triplicate and of each replicate 10,000 cells were measured.

5.2.5. Tetracycline staining

After 5 weeks of mineralization in osteogenic medium, 1% tetracycline was added to the medium for 24 h before fixation in 10% formalin (Sigma). 5 images from each sample, with 3 samples for each topography using a BD Pathway 435 automated fluorescence microscope. Integrated intensities were quantified using ImageJ software [41].

5.2.6. QPCR

Total RNA was isolated by using a RNA isolation kit (Bioline) according to manufacturer's protocol. 500 ng of RNA was used to prepare cDNA according to manufacturer's instructions in a 20 µl reaction volume (Biorad). Quantitative RT-QPCR was performed in a 20 µl reaction volume with 0.01 nmol of forward and reverse primers. 40 reaction cycles were performed which consisted of annealing at 60 °C for 15 s and extension at 72 °C for 15 s. Glycer-aldehyde 3-phosphate dehydrogenase (GAPDH) was used as a house-keeping gene and relative expression were determined using $\Delta\Delta\text{CT}$ method. Primer sequences are given in [Supplementary Table S3](#). Every experimental condition was performed in triplicate and of each replicate 2 QPCR reactions were performed.

5.3. In vivo experiments

5.3.1. Animal surgery

A total of 24 New Zealand White female rabbits from Dossy Biotechnology Ltd, Chengdu, China, were used. The weight of the animals was between 3000 and 3500 g. Housing of the animals and surgery was performed at Dossy Biotechnology Ltd, Chengdu, China. Animals were housed individually in cages in an environment with a temperature 16–28 °C and a humidity of 45–70%. Animals were fed *ad libitum* and are free to access water. Animals were observed per the standard monitoring schedule at Dossy Biotechnology. Before surgery, the Ti implants were sterilized by autoclave.

All procedures were approved by the local ethic committee for

the use of animals for studies and performed under general anesthesia and sterile conditions. The rabbits were sedated by intravenous application of pentobarbital sodium (3,0 mg/kg body weight).

Operation sites were shaved and sterilized with iodine and 70% EtOH and the animal was covered with a sterile blanket. Surgery was performed as described earlier [17,18] and illustrated in the [Supplementary Fig. S8](#). In short, a 5 cm incision on the proximal part of the femur was made, penetrating the epidermis, dermis and fascial layers exposing the underlying periosteum. An additional medial-anterior incision was made through the periosteum. The periosteum was elevated with a periosteal elevator. Two holes were made with a 1.0 mm twist drill (Stryker, Germany), using a custom made drill guide. With a custom made 7.05 mm diameter bur, a stable leveled site for the implants was made using the same drill guide. The implants were kept in place by a mesh plate (Endomed, The Netherlands). The subcutaneous layers were repositioned and layer by layer sutured with 4-0 silk suture. The surgical site was sterilized with iodine and animals were then placed in their cages and observed until awake and mobile. Wound healing was monitored daily. The rabbits were euthanized with an over-dose pentobarbital sodium (>3.0 mg/kg body weight). After euthanasia the femur with implant was removed and cleared from surrounding tissues. Bones with samples were then fixated in 10% neutral buffered formalin (>72 h s) and kept at 70% EtOH for further experiments. No incidents were registered during the course of animal experiments. For each time point (4 and 8 weeks) 12 rabbits were used. For each rabbit two implants were inserted in to each femur for a total of 4 implants per rabbit. From the resulting total of 8 replicates per topography, 4 were used for the pull-out tests and 4 were used for histological analysis. In addition to the fabricated titanium implants with designed topographies, sand blasted acid etched (SLA) implants (provided by Straumann, Switzerland) were included as a clinical benchmark and positive control.

5.3.2. Tensile test

The tensile test was performed using mechanical pull bench Adamel-Lhomargy DY-32 installed with a calibrated Sandoo SH-200 load cell of 0–200 N. PMMA cylinders were fabricated and fixed to the Ti implants using Cyanoacrylate glue, see [Supplementary Fig. S9](#). A through hole was drilled in the PMMA cylinder for connecting a 0.038 mm wire to the upper clamp. The pulling force was applied at 1 mm/min until the implant was removed from the bone.

5.3.3. Histology methods

Fixed samples were dehydrated in ethanol series and embedded in Methyl methacrylate (MMA). Sections were processed on a histological diamond saw (Leica SP1600) and stained with 1% Methylene Blue and 0,3% Basic Fuchsin solution. Three sections across the middle were made for each implant and scanned with a histologic slide scanner (Nanozoomer, Hamamatsu). For all sections the bone-implant contact percentage (%BIC) was measured. This is defined as all areas with direct bone contact to the implant without gaps or fibrous tissue. All samples were assessed by a blinded observer. To avoid confounding of the data, random measurements from the dataset were verified by two additional independent observers.

Acknowledgements

JdB, DS and FH gratefully acknowledge the financial support of the NanoNext NL (cluster 6C) initiative. JdB and AV acknowledge the financial support of the Dutch province of Limburg, AV the European Union's Seventh Framework Program (FP7/2007-2013) (grant agreement 289720). YZ thanks Peter Linders and Ite-Jan

Hoolsema from the Nanolab. Materiomics BV acknowledges Sip Jan Boorsma, Tom Buitenhuis, Peter Post, Andre Eppingbroek and Roy Kooijman, Techno Centrum voor Onderwijs en Onderzoek, University of Twente, Enschede and Harry Homan and Andre from Abbring, IMDS, Roden.

Appendix A. Supplementary data

Supplementary data related to this article can be found at <http://dx.doi.org/10.1016/j.biomaterials.2017.05.020>.

References

- [1] P. Drees, A. Eckardt, R.E. Gay, S. Gay, L.C. Huber, Mechanisms of disease: molecular insights into aseptic loosening of orthopedic implants, *Nat. Clin. Pract. Rheumatol.* 3 (Mar, 2007) 165.
- [2] S.S. Gao, Y.R. Zhang, Z.L. Zhu, H.Y. Yu, Micromotions and combined damages at the dental implant/bone interface, *Int. J. Oral Sci.* 4 (Dec, 2012) 182.
- [3] A.J. Engler, S. Sen, H.L. Sweeney, D.E. Discher, Matrix elasticity directs stem cell lineage specification, *Cell* 126 (Aug 25, 2006) 677.
- [4] Y. Mei, et al., Combinatorial development of biomaterials for clonal growth of human pluripotent stem cells, *Nat. Mater.* 9 (Sep, 2010) 768.
- [5] M.J. Dalby, et al., The control of human mesenchymal cell differentiation using nanoscale symmetry and disorder, *Nat. Mater.* 6 (Dec, 2007) 997.
- [6] W.L. Murphy, T.C. McDevitt, A.J. Engler, Materials as stem cell regulators, *Nat. Mater.* 13 (Jun, 2014) 547.
- [7] J. Lovmand, et al., The use of combinatorial topographical libraries for the screening of enhanced osteogenic expression and mineralization, *Biomaterials* 30 (Apr, 2009) 2015.
- [8] V. Kholodovych, et al., Prediction of biological response for large combinatorial libraries of biodegradable polymers: polymethacrylates as a test case, *Polymer* (2008) 2435–2439.
- [9] V. Kholodovych, et al., Accurate predictions of cellular response using QSPR: a feasibility test of rational design of polymeric biomaterials, *Polymer* 7367 (2004).
- [10] J. Kohn, W.J. Welsh, D. Knight, A new approach to the rationale discovery of polymeric biomaterials, *Biomaterials* 28 (Oct, 2007) 4171.
- [11] J.R. Smith, V. Kholodovych, D. Knight, W.J. Welsh, J. Kohn, QSAR models for the analysis of bioresponse data from combinatorial libraries of biomaterials, *QSAR Comb. Sci.* 24 (2005) 99.
- [12] A.L. Hook, et al., Combinatorial discovery of polymers resistant to bacterial attachment, *Nat. Biotechnol.* 30 (Sep, 2012) 868.
- [13] M. Hulshof, et al., Analysis of high-throughput screening reveals the effect of surface topographies on cellular morphology, *Acta biomater.* 15 (Mar, 2015) 29.
- [14] A. D. R. e. o. K. D. i. t. U. S. N. I. o. H, United States Renal Data System, National Institute of Diabetes and Digestive and Kidney Diseases, Bethesda, MD, 2014.
- [15] L. Hesse, et al., Tissue-nonspecific alkaline phosphatase and plasma cell membrane glycoprotein-1 are central antagonistic regulators of bone mineralization, *Proc. Natl. Acad. Sci. U. S. A.* 99 (Jul 09, 2002) 9445.
- [16] A.E. Carpenter, et al., CellProfiler: image analysis software for identifying and quantifying cell phenotypes, *Genome Biol.* 7 (2006) R100.
- [17] H.J. Ronold, J.E. Ellingsen, The use of a coin shaped implant for direct in situ measurement of attachment strength for osseointegrating biomaterial surfaces, *Biomaterials* 23 (May, 2002) 2201.
- [18] M. Monjo, S.F. Lamolle, S.P. Lyngstadaas, H.J. Ronold, J.E. Ellingsen, In vivo expression of osteogenic markers and bone mineral density at the surface of fluoride-modified titanium implants, *Biomaterials* 29 (Oct, 2008) 3771.
- [19] L. Sennerby, L.G. Persson, T. Berglund, A. Wennerberg, J. Lindhe, Implant stability during initiation and resolution of experimental periimplantitis: an experimental study in the dog, *Clin. Implant Dent. Relat. Res.* 7 (2005) 136.
- [20] M. Rocuzzo, N. De Angelis, L. Bonino, M. Aglietta, Ten-year results of a three-arm prospective cohort study on implants in periodontally compromised patients. Part 1: implant loss and radiographic bone loss, *Clin. Oral Implants Res.* 21 (May, 2010) 490.
- [21] A.D. Rape, M. Zibinsky, N. Murthy, S. Kumar, A synthetic hydrogel for the high-throughput study of cell-ECM interactions, *Nat. Commun.* 6 (Sep 09, 2015) 8129.
- [22] A.D. Celiz, H.C. Harrington, A.L. Hook, High throughput assessment and chemometric analysis of the interaction of epithelial and fibroblast cells with a polymer library, *Appl. Surf. Sci.* 313 (9/15, 2014) 926.
- [23] X. Li, et al., Micro-scaffold array chip for upgrading cell-based high-throughput drug testing to 3D using benchtop equipment, *Lab Chip* 14 (Feb 07, 2014) 471.
- [24] S. Gobaa, et al., Artificial niche microarrays for probing single stem cell fate in high throughput, *Nat. methods* 8 (Nov, 2011) 949.
- [25] H.V. Unadkat, et al., An algorithm-based topographical biomaterials library to instruct cell fate, *Proc. Natl. Acad. Sci. U. S. A.* 108 (Oct 4, 2011) 16565.
- [26] H. Yuan, et al., Osteoinductive ceramics as a synthetic alternative to autologous bone grafting, *Proc. Natl. Acad. Sci. U. S. A.* 107 (Aug 3, 2010) 13614.
- [27] A.M. Barradas, H. Yuan, C.A. van Blitterswijk, P. Habibovic, Osteoinductive biomaterials: current knowledge of properties, experimental models and biological mechanisms, *Eur. cells Mater.* 21 (May 15, 2011) 407.
- [28] J.E. Davies, Understanding peri-implant endosseous healing, *J. Dent. Educ.* 67 (Aug, 2003) 932.
- [29] R.K. Silverwood, et al., Analysis of osteoclastogenesis/osteoblastogenesis on nanotopographical titania surfaces, *Adv. Healthc. Mater.* 5 (Apr 20, 2016) 947.
- [30] N. Groen, et al., Exploring the material-induced transcriptional landscape of osteoblasts on bone graft materials, *Adv. Healthc. Mater.* 4 (Aug 05, 2015) 1691.
- [31] R. Olivares-Navarrete, et al., Mediation of osteogenic differentiation of human mesenchymal stem cells on titanium surfaces by a Wnt-integrin feedback loop, *Biomaterials* 32 (Sep, 2011) 6399.
- [32] C.H. Lohmann, et al., Surface roughness modulates the response of MG63 osteoblast-like cells to 1,25-(OH)₂D(3) through regulation of phospholipase A(2) activity and activation of protein kinase A, *J. Biomed. Mater. Res.* 47 (Nov, 1999) 139.
- [33] M. Aragona, et al., A mechanical checkpoint controls multicellular growth through YAP/TAZ regulation by actin-processing factors, *Cell* 154 (2013) 1047.
- [34] Y. Li, et al., Biophysical regulation of histone acetylation in mesenchymal stem cells, *Biophys. J.* 100 (Apr 20, 2011) 1902.
- [35] J. de Boer, et al., Inhibition of histone acetylation as a tool in bone tissue engineering, *Tissue Eng.* 12 (Oct, 2006) 2927.
- [36] T. Therneau, rpart: Recursive Partitioning and Regression Trees, 2014.
- [37] R. Core-Team, A Language and Environment for Statistical Computing, R Foundation for Statistical Computing, 2014. <http://www.R-project.org>.
- [38] K. Hornik, T. Hothorn, A. Zeileis, Unbiased recursive partitioning: a conditional inference framework, *J. Comput. Graph Stat.* (2006) 651–674.
- [39] W. A. L. A. M, Classification and regression by randomForest, *RNews* (December, 2002) 18–22.
- [40] M. Kuhn, Caret: Classification and Regression Training R Package Version 6.0-37, 2014. <http://CRAN.R-project.org/package=caret>.
- [41] R.S.J, M.P. Abramoff, Image processing with ImageJ, *Biophot. Int.* 11 (issue 7) (2004) 36–42.